Int. J. Electrochem. Sci., 16 **(2021)** Article ID: 210750, doi: 10.20964/2021.07.53

International Journal of
ELECTROCHEMICAL
SCIENCE
www.electrochemsci.org

Microwave-Modified Polyol Synthesis of a PtCo Electrocatalyst for the Oxygen Reduction Reaction in Acidic Electrolyte

M.A. Garcia-Contreras[1,*], *M. Gonzalez-Muñoz*[1,2]

[1] National Institute of Nuclear Research, Department of Chemistry, Carr. Mexico-Toluca S/N, Ocoyoacac 52750, State of Mexico, MEXICO.
[2] Polytechnical University of Toluca Valley, Almoloya of Juarez 50904, State of Mexico, MEXICO.
[*]E-mail: miguel.garcia@inin.gob.mx

Received: 14 March 2021 / *Accepted:* 4 May 2021 / *Published:* 31 May 2021

A microwave-assisted polyol synthesis was used to prepare a carbon-supported PtCo catalyst for the oxygen reduction reaction (ORR). The electrocatalyst was evaluated by a rotating disk electrode (RDE) technique in 0.1 M $HClO_4$ solution. Several analytical techniques were employed for physical characterization of the catalyst: X-ray diffraction (XRD), scanning electron microscopy (SEM), transmission electron microscopy (TEM) and energy-dispersive X-ray spectroscopy (EDX). Cyclic voltammetry (CV) curves were collected to calculate the electrochemically active surface area (ECSA) of the as-prepared catalyst. Compared to a Pt black catalyst, the as-prepared PtCo catalyst showed better ORR performance, with a higher exchange current. This performance can be explained by a synergistic effect ascribed to the nanostructure induced by heating with microwave radiation and the chemical dealloying process included in the preparation method. A reduction in ECSA was observed after an accelerated durability test (ADT), which was attributed to platinum dissolution and carbon corrosion processes.

Keywords: oxygen reduction; electrocatalyst; nanoparticles; polyol method; dealloying; microwave heating

1. INTRODUCTION

Fuel cell technology efficiently transforms the chemical energy of fuel to electricity. This technology is considered to be a promising alternative to internal combustion engines [1]. An electrocatalyst consisting of platinum metal on carbon is used to catalyze the two reactions that take place inside a proton exchange membrane fuel cell (PEMFC): the oxygen reduction reaction and hydrogen oxidation reaction (HOR) [2]. Unfortunately, platinum is an expensive and scarce metal, which has prevented the widespread commercialization of fuel cells. Therefore, the platinum loading in a fuel

cell must be low, for example, 20-40 g Pt in a Toyota Mirai fuel cell vehicle [3]. Furthermore, despite the extensive application of platinum in electrocatalysis, which is due to its relatively good stability [4], this metal does not completely resist degradation [4-6].

Consequently, the synthesis of very active and stable ORR electrocatalysts with low Pt loading has been a great challenge for the development of PEM fuel cells. It has been reported that several bimetallic Pt alloy catalysts are more active and less expensive than Pt alone [7-14] due to several factors, such as the Pt-Pt interatomic distance, number of nearest neighbors to Pt atoms, electron density in Pt 5d orbitals, surface roughness effects [15-21] and oxygen adsorption energy [22]. One way to reduce Pt loading in an electrocatalyst is to take advantage of the benefits of alloying Pt with nonnoble metals, such as transition metals [23-25]. It is well known that several factors are very important to obtain a good electrocatalyst, including particle size, shape, porosity, vacancies, electronic configuration, etc., which are greatly influenced by the preparation methods [26-27].

Among several synthetic approaches, the polyol process has been shown to be an efficient way to prepare catalysts, both unalloyed noble metals and noble metal-transition metal alloys of nanometric size [28-30], and it has been modified to prepare several binary electrocatalysts [31-35]. Such modifications include microwave (MW) heating since MW-assisted heating is an advanced technology that considerably reduces the reaction time in addition to promoting product yield and purity [36].

Microwaves can provide fast and stable heating of chemicals for use in reactions, such as reagents and solvents, as well as intermediate and final products. By using MW heating, the reduction of metal precursors and the nucleation of metal clusters that induce the formation of monodispersed nanoparticles can be performed more quickly.

Materials with high crystallinity can be prepared with MW heating since it is a fast and uniform process [37-38]. The MW-assisted synthesis method has been employed to prepare several catalysts [39-43]. In this study, a microwave-assisted polyol (EG) synthesis and a two-step precipitation method were utilized to prepare a PtCo/C catalyst. The synthesis method included thermal treatment and chemical dealloying steps. The ORR activity was evaluated with a rotating disk electrode technique in 0.1 M $HClO_4$ electrolyte solution. Kinetic parameters for the ORR were obtained from Koutecky-Levich analysis, and a commercial Pt black catalyst was evaluated for comparison.

2. EXPERIMENTAL

2.1. Preparation of catalyst

PtCo/C was prepared by a microwave-assisted modified polyol method. The synthesis procedure was carried out as follows: cobalt acetate was added to a solution of Vulcan XC-72R (Cabot Corp.) carbon in ethylene glycol after sonication for 30 minutes with an argon sparge. Afterwards, 0.5 M NaOH in EG was added while stirring to adjust the pH to 11.0. A solution of 12 wt.% $NaBH_4$ in 14 M NaOH (Aldrich) was added dropwise while stirring and maintaining the argon flow. Several cycles (10 s ON, 20 s OFF) were performed in a MW oven (Household Samsung 800 W) to heat the solution to 135 °C; between cycles, the temperature was measured while the solution was stirred and sparged with Ar. Afterwards, 5 more cycles (5 s ON, 20 s OFF) were carried out. This mode of MW heating was used to

prevent EG from boiling. After washing with ethanol several times and centrifuging at 4,000 rpm for 10 minutes, the resulting cobalt nanoparticles were dried at 100 °C for 2 hours in a tubular furnace with an argon flow. In the next step, K_2PtCl_4 and 30 ml of EG were added to a beaker while stirring and sparging with argon for 20 minutes. The as-prepared cobalt particles were added to another beaker under the same conditions. K_2PtCl_4 in EG solution was added slowly to the Co suspension while stirring and sparging with argon during all processes. A $NaBH_4$ solution was added dropwise. The MW cycles and the washing and drying procedures were repeated. Thermal treatment at 200 °C with an argon flow for 2 hours was applied to the obtained PtCo/C catalyst. After cooling, PtCo/C catalyst nanoparticles were placed in a beaker containing 0.5 M H_2SO_4 at 40 °C for 2 hours while stirring and sparging with argon. This step was performed because other investigations reported that dealloyed bimetallic nanoparticles were very active and stable electrocatalysts for the ORR. Dealloying is the selective removal of a less noble component from a bimetallic alloy to modify its surface properties [44]. Finally, the particles were washed with deionized (D.I) water several times and dried to collect the PtCo catalyst. The nominal catalyst composition was 20 wt% Pt+Co and 80 wt% Vulcan XC-72R, with a Pt:Co weight ratio of 3:1 and BH_4:metal precursor weight ratio of 2:1. Figure 1 shows a flow diagram for the synthesis of the PtCo/C electrocatalyst.

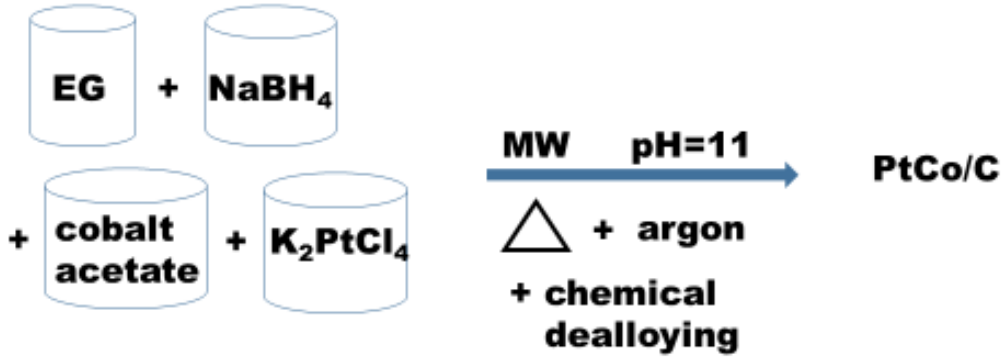

Figure 1. Flow diagram for the synthesis of PtCo/C

2.2. Physical characterization

Physical characterization was carried out by X-ray diffraction with a Bruker D8 Discover diffractometer using a CuKα radiation source. The range between 15° and 100° was scanned at 1.4° min^{-1} in steps. The average crystallite size was calculated by measuring the full width at half maximum (FWHM) in the XRD pattern of the (220) plane and using Scherrer's equation. EDX analysis of the PtCo/C catalyst was performed with a JEOL JSM-5600LV scanning electron microscope. A voltage of 20 kV was used to calculate the chemical composition. To obtain more information about the catalyst morphology and to compare crystallite size calculations, transmission electron microscopy (TEM, JEOL JEM 2000 FXII) with an accelerating voltage of 200 kV was utilized, and several micrographs were obtained. TEM analysis provided data on nanoparticle size and morphology.

2.3. Electrode preparation and electrochemical experiments

Preparation of working electrodes was carried out taking into consideration several reports about the optimization of catalyst ink composition and standardizing RDE methodology, which includes several factors that influence catalyst performance in different ways [45-52]. These investigations report the importance of each step for the following:

i) Catalyst ink composition
ii) Polishing and cleaning of the working electrode
iii) Electrochemical cell cleaning
iv) Catalyst loading range
v) Catalyst ink sonication
vi) Drying procedure for working electrodes
vii) Potential scan rates for cyclic and linear voltammetry.

In this work, the ink formulation is reported for clarity: 3 mg of PtCo/C catalyst was mixed with 4.2 µl of Nafion (5 wt.% in water/aliphatic alcohol solution, Aldrich), 210 µl of isopropanol + 835.8 µl of deionized water (5 MΩ cm^{-1}) and sonicated for 30 minutes. The catalytic ink was homogenized with treatment in an ultrasonic bath, and the working electrode was prepared by depositing 8 µl of catalytic ink on a mirror-finished glassy carbon disk (5 mm diameter); hence, 16.3 µg cm^{-2} Pt was loaded on the RDE. The working electrode was dried in air overnight. For comparison, a Pt black (ALFA AESAR) electrode was prepared with a Pt load of 16 µg cm^{-2}. Electrochemical experiments were performed at 25 °C in Ar-purged (UHP, INFRA) or O_2-saturated (UHP, INFRA) 0.1 M $HClO_4$ supporting electrolyte in deionized water utilizing a typical three-electrode electrochemical cell. A Hg/Hg_2SO_4 electrode and a Pt mesh were used as reference and counter electrodes, respectively. Here, all potentials were referenced to the normal hydrogen electrode (NHE). The electroactive surface area (EAS) was estimated by integrating the charge in the H_2 adsorption-desorption section (ORIGIN 8.1 software) of a cyclic voltammogram obtained at a sweep rate of 50 mVs^{-1} in argon-saturated 0.1 M $HClO_4$ after the working electrode was activated with 20 cycles from 0.0 to 1.0 V vs. NHE. Polarization curves were obtained to assess oxygen reduction activity at a sweep rate of 10 mVs^{-1} and rotation speeds from 400 to 2500 rpm in O_2-saturated 0.1 M $HClO_4$ electrolyte solution. A bipotensiostat (PINE Model AFCBP1) and a rotator (PINE Model 636) were employed for electrochemical experiments.

3. RESULTS AND DISCUSSION

3.1. Physical characterization

Powder XRD patterns for the PtCo/C catalyst were obtained and analyzed according to the powder diffraction standard files (PDF). Since XRD is a bulk method, it provides information on the catalyst bulk structure. The XRD pattern of PtCo/C is shown in Fig. 2. The wide reflection at 25° (002) corresponds to the Vulcan XC-72 carbon black support and suggests that it has good graphitic

characteristics. In the XRD pattern of PtCo/C, there is no Co peak, which suggests that $CoPt_3$ is formed or that cobalt is in the core. In Fig. 2, Pt (111), (200), (220), (311) and (222) planes occur close to the standard 2θ values of 40.04°, 46.535°, 67.861°, 81.506° and 85.95° (PDF 01-1194), respectively; however, structural effects shift the positions of the peaks to 40.28°, 46.71°, 68.23°, 82.24° and 86.8°, respectively, which are close to the peaks for the $CoPt_3$ phase (PDF 29-0499) at 40.52°, 47.12°, 68.84°, 83.04° and 87.64°. It could be inferred that cobalt metal atoms remained isolated in PtCo and formed an alloy only with atoms that were present on the surface of the core [53].

The mean crystallite size for the catalyst was calculated by using Scherrer's equation [54], Eq. (1), based on the (220) reflection [55].

$$L = k\lambda / \beta \cos \theta \quad (1)$$

where L = mean particle size
k = constant = 0.94
λ = X-ray wavelength =1.54 Å
θ = diffraction angle of (220) peak
β = half-peak broadening of (220) peak

$$\lambda = 2d \sin \theta \quad (2)$$

The lattice parameter ($a= [d^2 (h^2 + k^2 + l^2)]^{1/2}$ was calculated from Bragg's law, Eq. (2), and h, k, and l values of the (220) plane to estimate the degree of alloying in the catalyst.

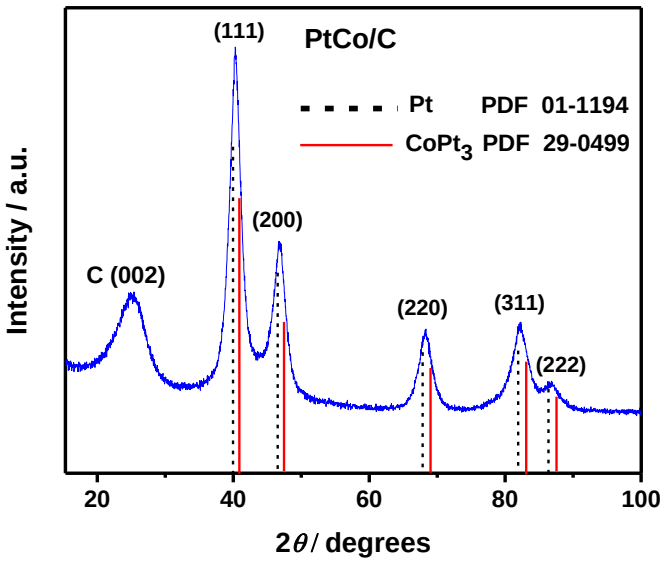

Figure 2. XRD pattern of the as-prepared PtCo/C catalyst.

A decrease in lattice parameter was shown by PtCo/C (3.883) in comparison with Pt (3.9161 Å), which suggested an improvement in the Co-Pt interaction and indicated that the level of alloying was enhanced while the Pt-Pt interatomic distance was reduced [56]. The shift in the 2θ value and the reduction in the lattice parameter from the Pt XRD pattern was attributed to a structural effect supporting the formation of a core-shell morphology [53]. Fig. 3 shows SEM micrographs of the as-prepared PtCo/C catalyst supported on a Vulcan XC-72 carbon matrix. In these images, Pt-Co nanoparticle aggregates with a uniform distribution can be observed. The inset of Fig 3(a) depicts the EDX analysis, and the wt.% of Co/Pt is determined to be 27:90, which is a good approximation to the nominal proportion of 1:3.

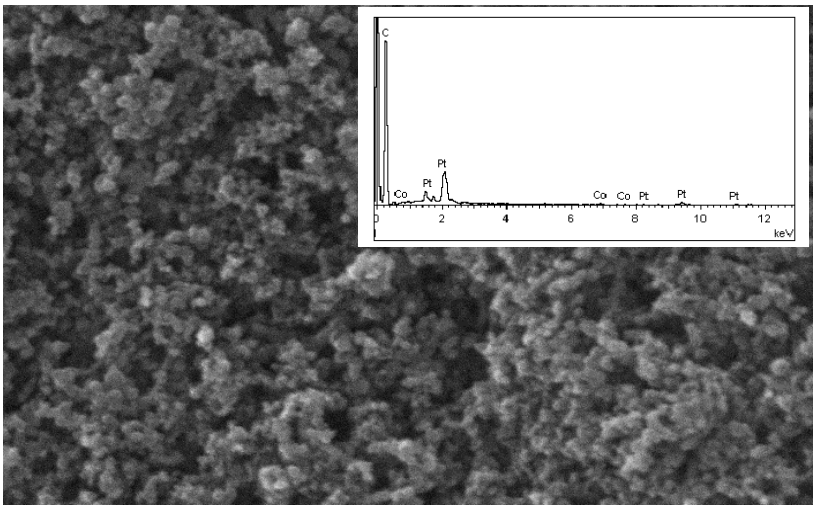

Figure 3. SEM images of the PtCo/C catalyst on a Vulcan carbon matrix. Inset: EDX analysis spectrum.

Fig. 4 depicts TEM images of the PtCo/C catalyst. The contrast in brightness shows that there are distinct elements present on the carbon support. Fig 4(c) displays a core-shell structure since a contrast can be observed due to differences in atomic numbers, where Co (z=27) has lower intensity (cores), and Pt (z=78) has higher intensity (shells) [52]. Fig. 4(c) shows a particle with a 1.2-nm shell and a 3.8-nm core. Fig. 4(d) shows the associated selected area electron diffraction (SAED) pattern. The major diffraction rings were indexed to match those identified by XRD. The discrepancy between the mean particle sizes determined by TEM and XRD was ascribed to the fact that XRD only considers crystalline particles without studying the real morphology of the catalyst [57]. Table 1 shows the physicochemical parameters of the PtCo/C electrocatalyst.

Table 1. Physico-chemical parameters of the PtCo/C electrocatalyst

Nominal ratio (wt.%) Co:Pt	Chemical composition (EDX) (wt. %) Co:Pt	Lattice parameter (Å)	Crystallite size (nm)	TEM particle size (nm)
1:3	27:90	3.883	4.5	7.3

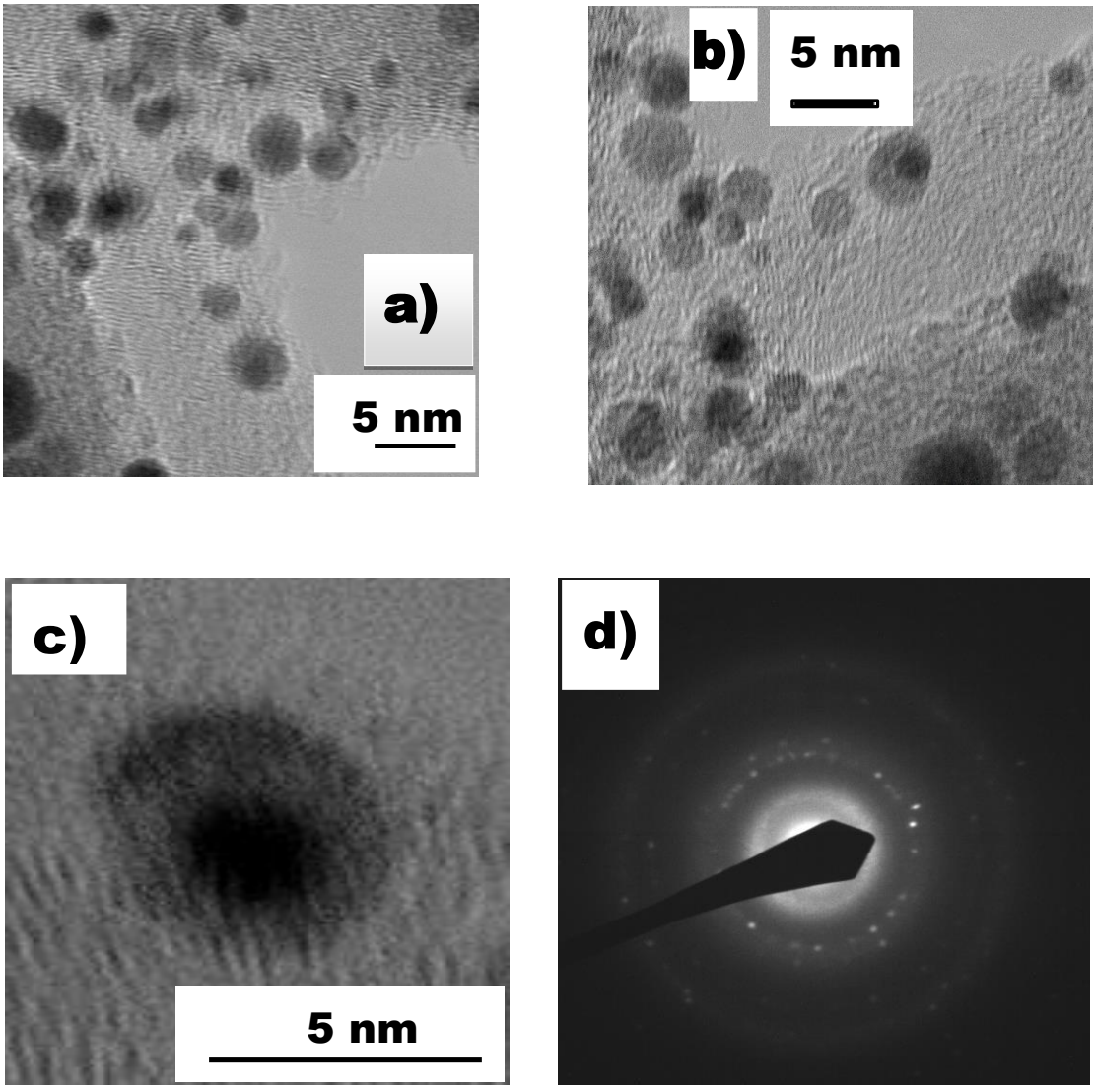

Figure 4. TEM images of the PtCo/C electrocatalyst: **a)** and **b)** PtCo/C nanoparticles; **c)** Core-shell nanostructure with a 1.2-nm Pt shell and a 3.8-nm Co core; **d)** The associated selected area electron diffraction (SAED) pattern.

3.2. Electrochemical measurements

The CV curve of the PtCo/C electrocatalyst was obtained in the supporting electrolyte 0.1 M $HClO_4$ at a sweep rate of 50 mV s^{-1}; it is presented in Fig. 5 and compared with the Pt black catalyst CV curve. The stabilized curves obtained after 20 cycles were used to calculate the EAS by considering the charge associated with hydrogen adsorption/desorption process (first zone in the cyclic voltammogram) and using a factor of 210 μC cm^{-2} for the adsorption of a hydrogen monolayer on Pt [58]. With Eq. (3), ECSA of PtCo/C catalyst can be estimated:

$$ECSA = Q_H / L_{Pt} \times 0.21 \quad (3)$$

where L_{Pt} = Pt loading, μg cm^{-2}
Q_H = charge exchanged during the electrodesorption of hydrogen on a Pt surface, mC cm^{-2}
0.21 = charge required to oxidize a monolayer of hydrogen on smooth Pt, mC cm^{-2} [59]

Figure 6 shows the polarization curves for the ORR on the PtCo/C electrocatalyst in O_2-saturated 0.1 M $HClO_4$ solution with a sweep rate of 10 mV s^{-1} and rotation rates from 400 to 2500 rpm. The high onset potential for ORR (~ 0.9 V vs. NHE) and half-wave potential of 700 mV at 1600 rpm suggest good activity of the PtCo/C catalyst.

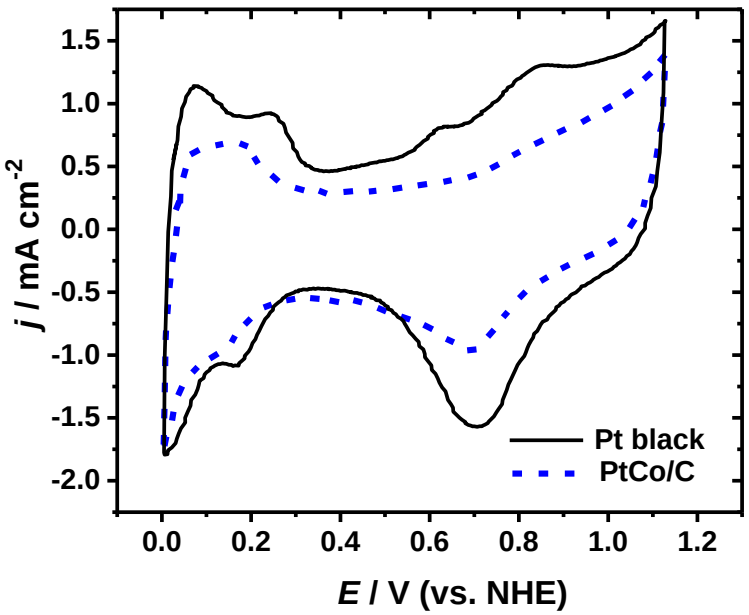

Figure 5. Cyclic voltammograms of PtCo/C and Pt black catalysts in 0.1 M $HClO_4$ electrolyte with a scan rate of 50 mVs^{-1} at 25 °C.

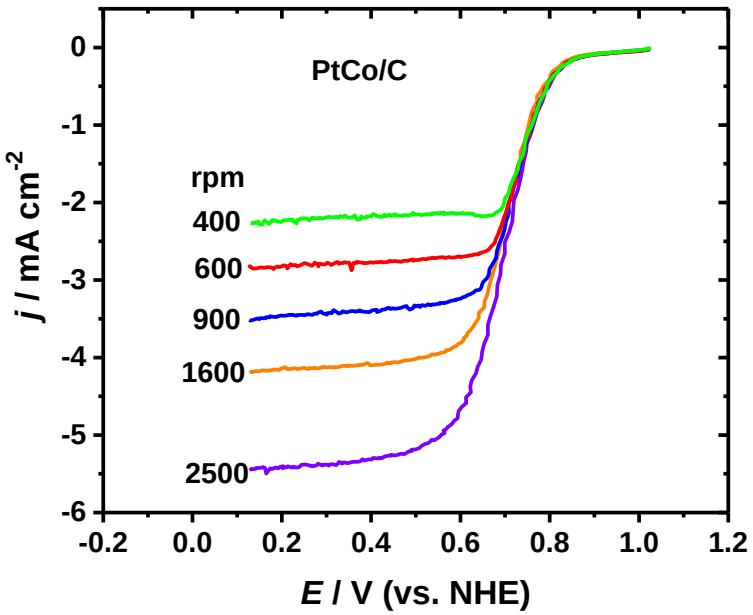

Figure 6. Hydrodynamic voltammograms for the ORR on the PtCo/C catalyst using RDE in O_2-saturated 0.1 M $HClO_4$ solution with a scan rate of 10 mVs^{-1}.

In Fig. 6 three distinct zones can be observed. First, there is a region where the charge transfer control can be seen from 0.9 to 0.82 V vs. NHE. Second, a mixed-control zone is located from 0.82 to 0.65 V vs. NHE, where kinetic- and diffusion-limited processes control the current density. Third, the diffusion-limited region is in the range from 0.62 to 0.15 V vs. NHE. As expected, the ORR curves are shifted to higher currents as the rotation speeds increase. At 2500 rpm, the limiting current density is approximately -5.5 mA $cm^{-2}_{(geom.)}$. A Koutecky-Levich plot, which displays the inverse of the overall current density (j -1) vs. the inverse square root of the rotation rate ($\omega^{-1/2}$)m is presented in Fig. 7. A linear relationship between j^{-1} and $\omega^{-1/2}$ can be observed, indicating first-order kinetics for the ORR on this catalyst. With a diffusion-limited current density, j_d, a Levich plot was drawn, as shown in Fig. 7. From the slopes of the Levich curves, the number of transferred electrons, *n*, for the ORR was calculated by using Eq. (4):

$$j_d = 0.62\, n\, F\, D_{O2}^{2/3}\, C_{O2}\, \omega^{1/2}\, v^{-1/6} = B\, \omega^{1/2} \quad (4)$$

where

0.62 = a constant when ω is expressed in rad s^{-1}

F = Faraday's constant = 96845 C mol^{-1}

D_{O2} = oxygen diffusion coefficient in 0.1 M $HClO_4$ = 1.7 x 10-5 cm^2 s^{-1} [60]

v = kinematic viscosity of electrolyte = 1. 009 x 10^{-2} cm^2 s^{-1}

ω = rotation speed expressed in rad s^{-1}

C_{O2} = oxygen concentration in the electrolyte = 1. 26 x 10- 3 mol L^{-1} [61]

B = a parameter obtained from slopes of the straight lines in the Koutecky-Levich plot.

The theoretical *B* parameter obtained with Eq. (4) for the ORR through 4-electron transfer was 0.4288 mA cm^{-2} $(rad/s)^{-1/2}$, and the slopes of the linear regression were very similar in the potential interval from 0.48 to 0.62 V vs. NHE, such that the number of exchanged electrons *n* was determined to be 3.8. This value suggests that the ORR mechanism changed slightly due to the surface composition impacting the catalyst features.

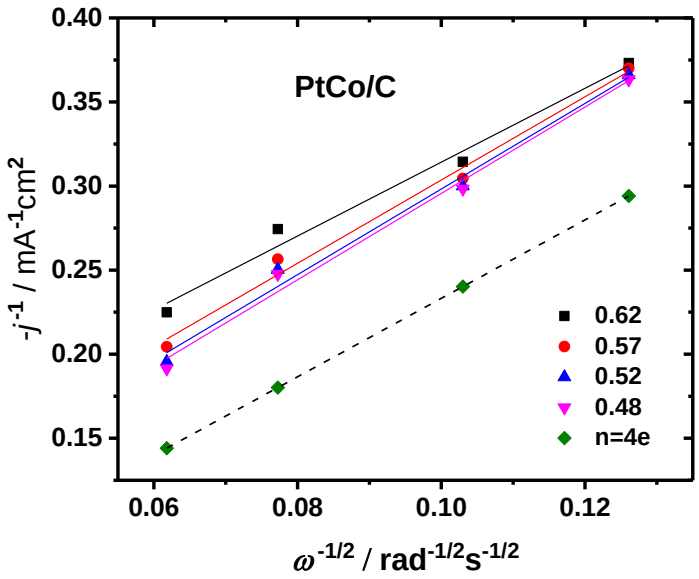

Figure 7. Koutecky-Levich plot for the PtCo/C catalyst at various potentials in O_2-saturated 0.1 M $HClO_4$ solution with a sweep rate of 10 mVs^{-1}.

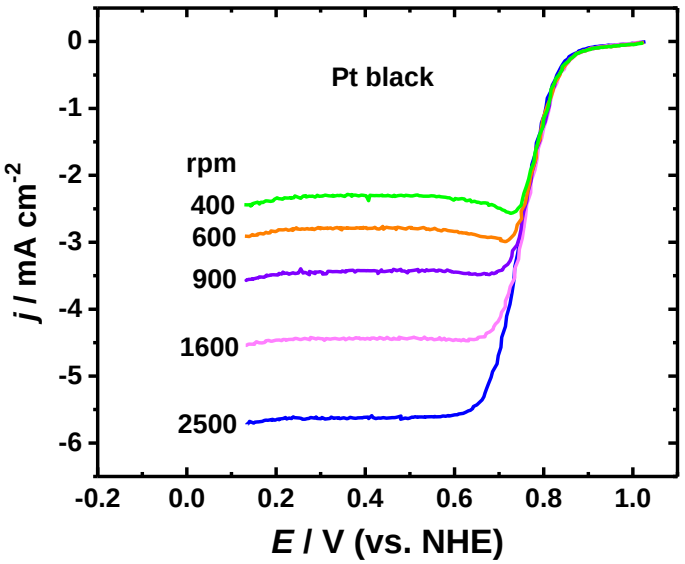

Figure 8. ORR polarization curves on the Pt black catalyst in O_2-saturated 0.1 M $HClO_4$ solution at 10 mV s^{-1}

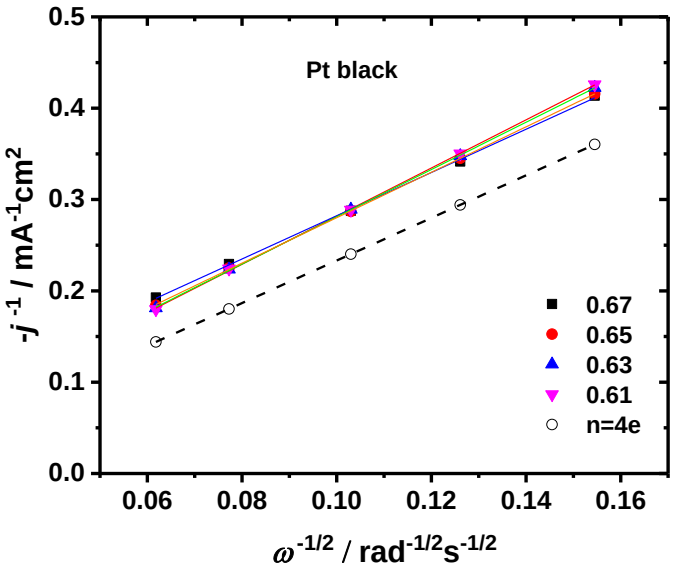

Figure 9. Koutecky-Levich plot for Pt black catalyst at various potentials in O_2-saturated 0.1 M $HClO_4$ solution with a sweep rate of 10 mVs^{-1}.

Accordingly, ORR polarization curves on the Pt black catalyst in O_2-saturated 0.1 M $HClO_4$ solution and Koutecky-Levich plots for the Pt black catalyst at various potentials are shown in Fig. 8 and Fig. 9, respectively.

From Figs. 6-9, Tafel curves were constructed; that is, graphs were corrected for mass transfer, as shown in Fig. 10. A Tafel plot consists of two zones, one with low current density and the other with high current density, and both regions have different slopes. In Tafel curves, the kinetic current density, j_k, is calculated from Koutecky-Levich analysis [62]. In this study, the Tafel slopes in the low current zone were 103 and 134 mV dec^{-1} for the Pt black and PtCo/C catalysts, respectively. The theoretical Tafel slope values are 60 mV dec^{-1} for the low current density zone and 120 mV dec^{-1} for the high current density region; the differences in this study could be attributed to species that obstruct the active catalytic sites. The Tafel slope of an electrochemical reaction is an intrinsic feature of the electrode kinetics and includes several basic stages, such as noninteracting adsorption (a Langmuir isotherm) and a rate-limiting step (RLS). Changes in the ORR kinetic behavior have been ascribed to modifications in the coverage of the surface by adsorbed oxygen-containing intermediate species, such as OOH, O, and OH. These species come from water and O_2 [63,64]. For the ORR, Tafel slopes have been reported in the range of 150-215 mV dec^{-1} in the high-overpotential region when there has been some level of surface coverage by adsorbed hydroxyl ions [56]. Table 2 presents the kinetic parameters of the PtCo/C catalyst studied in this work. The PCo/C and Pt black catalysts exhibited mass activities of 0.121 and 0.19 A mg Pt^{-1} at 0.9 V vs. NHE, respectively (whereas that of a commercial Pt/C catalyst is 0.2 A mg Pt^{-1}) [58].

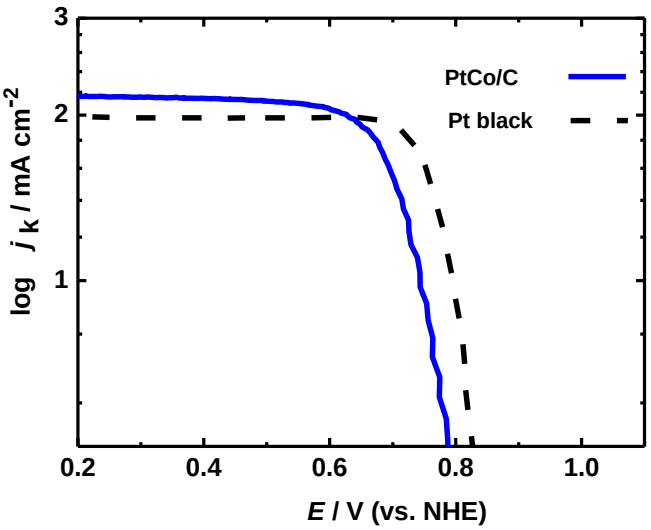

Figure 10. Mass-transfer-corrected Tafel plots for O_2 reduction on PtCo/C and Pt black catalysts in O_2-saturated 0.1 M $HClO_4$ electrolyte.

Table 2. Kinetic parameters from the oxygen reduction polarization curves on PtCo/C and Pt black electrocatalysts in 0.1 M $HClO_4$ solution at 25 °C.

	PtCo/C	**Pt black**
$B_{teo.\ 4e^-}$ / mA^{-1}cm^2(rad/s)$^{-1/2}$	0.4288	0.4288
B_{exp} / mA^{-1}cm^2(rad/s)$^{-1/2}$	0.40873	0.3968
ne^-	3.8	3.7
b / mV dec^{-1}	134	103
j_o / mA cm$^{-2}_{geom.}$	2.62 x 10^{-4}	6 x 10^{-5}
j_k @0.9 V / mA cm$^{-2}_{geom.}$	0.086	0.113
ECSA / m^{2}g^{-1} before ADT/after ADT	28.25 / 17.71	168.74 / 62.34
MA @ 0.9 V / A mg$_{Pt}^{-1}$	0.121	0.19
ORR onset potential / V	0.83	0.9
half-wave potential / V	0.7	0.77
Activity loss after ADT @ 1600 rpm / %	5.18	6.13

Table 3 depicts the performance of several PtCo electrocatalysts for the oxygen reduction reaction and is discussed here. $PtCo_3$ was synthesized by the impregnation method, followed by freeze drying and thermal annealing in a reductive atmosphere, with additional treatment at 800 °C. XRD patterns of the alloys exhibited a disordered face-centered cubic (fcc) lattice-type structure. Afterwards, electrochemical dealloying was performed with fast voltammetric cycling to induce the enrichment and availability of Pt atoms on the particle surfaces. This $PtCo_3$ catalyst showed significantly enhanced specific current density and mass activity due to geometric and compressive lattice strain effects of the dealloyed Pt-Co nanoparticles [65]. PtCo was prepared by microwave-assisted polyol synthesis with

thermal pretreatment, and crystalline particles of 2.4 nm were obtained. Alloying was confirmed with the shift of peaks to lower angles in the XRD pattern due to the smaller size of cobalt atoms. After electrochemical evaluation by using the RDE technique, kinetic parameters such as the number of transferred electrons, limiting current density, Tafel slope and exchange current density were estimated [66]. A PtCo nanoelectrocatalyst was synthesized via a solvothermal method with ethylenediamine as the solvent and bidentate ligand, $NaBH_4$ as the reducing agent and poly(vinyl pyrrolidone) as the surfactant. This process produced an interesting nanodendritic structure that exhibited enhanced specific and mass activities in comparison with those of a commercial Pt/C catalyst [67]. Pt-Co nanocatalysts composed of ordered Pt_3Co intermetallic cores with a 2-3 atomic-layer-thick Pt shell were synthesized by an impregnation method and thermal treatment at 700 °C under a H_2 atmosphere. These nanocatalysts showed remarkable mass activity and minimal loss of activity after a durability test of 5,000 potential cycles. Their high performance could be explained by a stable core-shell intermetallic arrangement, with better activity for the 700 °C catalyst [68]. A one-pot hydrothermal method was used to prepare PtCo nanoparticles embedded in nitrogen-doped graphene nanopores (PtCo/NPG) through direct etching by platinum and cobalt precursors in pristine graphene. The catalyst was finally annealed under a N_2 atmosphere at 700 °C for 2 h to yield a PtCo/nanohybrid. Characterization by electron microscopy (TEM and SEM) revealed an almost transparent graphene film with many nanopores, with an average diameter of 3-10 nm. The XRD pattern showed that the reflections of PtCo/NPG shifted to higher angles, indicating that Co atoms were incorporated into the Pt lattice to form an alloy phase. ORR activity was investigated in alkaline and acidic media, with lower performance observed in 0.1 M $HClO_4$, which was attributed to poisoning of the nitrogen-doped structure by the electrolyte [69]. A laser ablation synthesis was developed to prepare spherical PtCo nanoalloys with controllable size, atomic compositions and degrees of alloying. These results were achieved by adjusting the precursor salt concentrations, pH conditions and ablation times. Several PtCo alloy catalysts were obtained with a Pt loading of 19-21 μg cm^{-2}, ECSA = 14-31 m^2g^{-1}, specific activity 0.38-1.18 mA cm^{-2} and 0.06-0.28 mA μg_{Pt}^{-1} in 0.1 M $HClO_4$. These excellent ORR activities are attributed to a thin layer of Pt-rich shell on an alloy core [70]. Pt-Co alloy nanocrystals on a support of reduced graphene oxide were previously synthesized by a solvothermal process with glycine and PVP as a structural-modifying agent and surfactant, respectively, which influenced the morphology and yielded nanocubic catalysts with high-index facets. The ORR activity was investigated in that study, and the specific activities were 0.67-1.53 mA cm^{-2} [71]. It can be observed from the data in Table 3 that, as has been reported, methods to synthesize catalysts involve many conditions and factors; these methods are crucial for designing and obtaining materials for efficient electrocatalytic applications, in our case, the oxygen reduction reaction. Morphology, structure, composition, supports, etc., can be tailored in such a way to influence the strain lattice, 5d vacancies, and electronic effects to yield high-performance and durable catalysts.

Table 3. ORR activities of different catalysts at 0.9 V vs. RHE

Catalyst	Preparation method	Electrolyte solution	Specific activity (mA cm^{-2})	Mass activity (A mg_{Pt}^{-1})	Exchange current (mA cm^{-2})	Ref.
$PtCo_3$	Impregnation, annealing and dealloying	0.1 M $HClO_4$	0.804	0.38	---	65
PtCo	Microwave-assisted polyol	0.1 M $HClO_4$	----	---	1.21 E^{-05}	66
PtCo	Solvothermal	0.1 M $HClO_4$	0.68	0.11	---	67
PtCo	Impregnation, thermal treatment 400 °C 700 °C	0.1 M $HClO_4$	0.31 1.12	0.15 0.52	---	68
PtCo/NPG	Hydrothermal, annealing	0.1 M $HClO_4$	0.15	---	---	69
PtCo	Ablasion laser	0.1 M $HClO_4$	1.18	0.28	---	70
PtCo/rGO	Solvothermal	0.1 M $HClO_4$	1.53	---	---	71
PtCo	Microwave-modified polyol	0.1 M $HClO_4$	---	0.12	2.62 x 10^{-4}	This work

To determine the stability of the PtCo/C catalyst, an accelerated durability test (ADT) was performed with 10,000 potential cycles at a sweep rate of 50 mVs^{-1} in the 0.6-1.0 V range vs. NHE with argon-saturated 0.1 M $HClO_4$ electrolyte at 25 °C. The experimental conditions of ADT mimic idling and open-circuit conditions when a fuel cell is operating at low and high current densities [72].

Fig. 11 shows cyclic voltammograms of the PtCo/C electrocatalyst in 0.1 M $HClO_4$ solution before and after ADT, which led to a 37% reduction in the electroactive surface area. Fig. 12 exhibits linear voltammograms of the PtCo/C electrocatalyst at a rotation rate of 1600 rpm before and after ADT; the ORR polarization curve after ADT showed a 5.18% reduction in current density (geom.) and a decrease in the half-wave potential of 80 mV. A reduction in EAS after ADT was observed for the PtCo/C catalyst and was be attributed to the predominant degradation mechanisms, such as a) Ostwald ripening, which induces a particle size increase via a dissolution-redeposition effect by redox cycling, b) agglomeration (so-called sintering or coalescence) of particles, and c) corrosion of the carbon support

catalyzed by platinum, resulting in removal of Pt particles from the support and subsequent agglomeration [73].

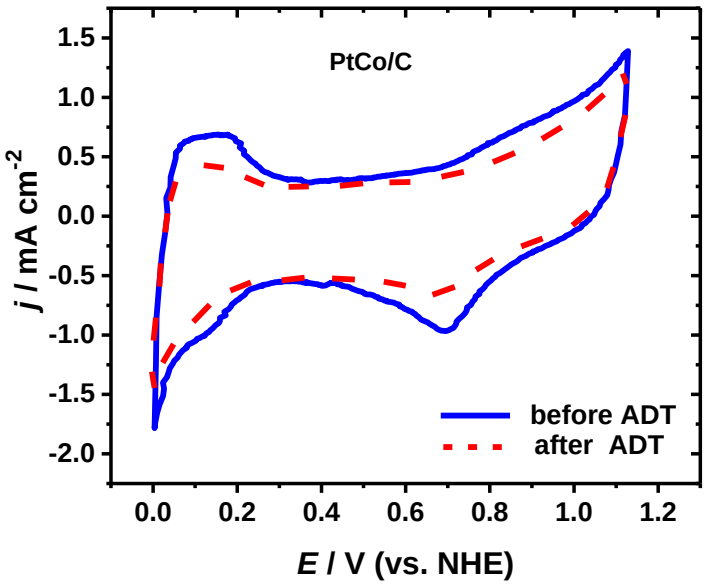

Figure 11. Cyclic voltammograms of the PtCo/C catalyst before and after the accelerated durability test.

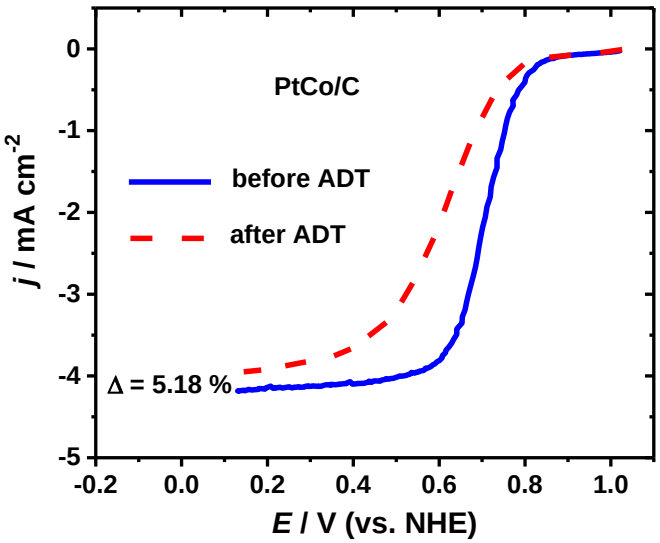

Figure 12. ORR polarization curves on the PtCo/C catalyst at 1600 rpm in O_2-saturated 0.1 M $HClO_4$ solution before and after the accelerated durability test.

There are several factors that can reduce catalyst stability, such as a broad distribution of sizes, since it may induce Ostwald ripening, where smaller Pt particles (with a higher chemical potential) tend to dissolve more rapidly [74]. A reduction in EAS clearly ascribed to Pt nanoparticle agglomeration after ADT has been reported, and for 2-nm particles, an EAS reduction of 55% was found [72]. Furthermore, carbon monoxide that formed on the carbon support surface at potential values > 0.3 V vs. NHE can be

oxidized to CO_2 at potential values between 0.6 and 0.8 V through Pt activation to catalyze this oxidation reaction. Therefore, it can be inferred that part of the carbon corrosion process is induced by platinum, and it takes place very close to Pt sites, causing a detrimental effect on Pt-carbon support interactions. The consequences are surface damage and reduction in the number of catalytic Pt sites. This process occurs in the same potential interval as the ORR, and thus, it is technically very important [75].

In summary, in the present investigation, a PtCo/C electrocatalyst was synthesized with a combined method according to valuable guidance from reported investigations, as indicated in the Experimental section. Physical characterization showed that a PtCo/C catalyst was obtained with a crystalline structure and a morphology of agglomerated nanoparticles as a result of the combined effects of several preparation steps: microwave heating; enhanced reduction by a strong reducing agent, $NaBH_4$; and chemical dealloying through acid leaching for an optimized time (2 h), as reported elsewhere [76]. Thermal treatment supported the formation of the alloy. The electrochemical measurements revealed good ORR activity, consistent with results reported for Pt alloys due to electronic, ligand and geometric effects, but not as high as results for the Pt black catalyst, except for the exchange current, where a value of 2.62 10^{-4} mA $cm^{-2}_{(geom.)}$ was found, in comparison to 6 10^{-5} mA $cm^{-2}_{(geom.)}$ for the Pt black catalyst. A Tafel slope steeper than the theoretical value (134 vs. 120 mV dec^{-1}) was obtained, which could be attributed to some intermediate species blocking the active sites of the catalyst. A decrease of 37.3% in EAS after ADT was found, and based on the current literature, catalyst degradation could have been caused mainly by platinum dissolution and carbon corrosion phenomena. To decrease the corrosion of the carbon support, other materials such as graphitized carbon, carbon nanotubes, or ceramic have been found to be efficient supports [77-79].

4. CONCLUSIONS

A microwave-modified polyol synthesis was performed to obtain a PtCo/C electrocatalyst. The ORR performance was quantitatively investigated by using RDE measurements and reported through kinetic parameters. A Pt black catalyst was used as a reference. The electrochemical measurements showed that this PtCo/C catalyst had good ORR activity, with an exchange current higher than that observed for a Pt black control; the synthesized material had a polycrystalline structure, obtained through the combined synergistic effects of microwave heating, metal reduction by a strong agent, thermal treatment and chemical dealloying. A decrease in the electroactive surface area was observed after accelerated durability testing, which was attributed to platinum dissolution and carbon corrosion processes.

ACKNOWLEDGEMENTS
The authors thank P. Lopez, I. Martinez, M. Espinosa and J. Martinez for the XRD, SEM and TEM images.

CONFLICT OF INTEREST
The authors declare that they have no conflict of interest.

References

1. Y. Wang, D.F. Ruiz, K.S. Chen, Z. Wang, X.C. Adroher, *Mater.* Today, 32 (2020) 178.
2. O. Sekizawa, T. Kaneko, K. Higashi, Sh. Takao, Y. Yoshida, T. Gunsi, X. Zhao, G. Sanjeke, T. Sakata, T. Uruga, Y. Iwasawa, *Top. Cat*., 61 (2018) 889.
3. O Gröger, H.A. Gasteiger, J.P. Suchsland*, J. Electrochem. Soc.*, 162 (2015) A2605.
4. S. Cherevko, N. Kulyk, K.J.J. Maryhofer, *Nano Energy*, 29 (2016) 275.
5. A. Pavlisic, P. Jovanovic, V. S. Selih, M. Sala, N. Hodnik, M. Gaberscek, *J. Electrochem. Soc.*, 165 (2018) F3161.
6. M. Pourbaix, *Atlas of electrochemical Equilibria in Aqueous Solutions*. National Association of Corrosion Engineers (1974)
7. N. Todoroki, R. Kawamura, M. Asano, R. Sasakawa, Sh. Takahashi, T. Wadayama, *Phys. Chem. Chem. Phys.*, 20 (2018) 11994.
8. U.A. Paulus, A. Wokaun, G.G. Scherer, T.J. Schmidt, V. Stamenkovic, V. Radmilovic, N.M. Markovic, P.N. Ross, *J. Phys. Chem. B,* 106 (2002) 4181.
9. M. Min, J. Cho, K. Cho, H. Kim, *Electrochim. Acta,* 45 (2000) 4211.
10. L.G.R.A. Santos, K.S. Freitas, E.A. Ticianelli, *Electrochim. Acta*, 54 (2009) 5246.
11. M. Huang, L. Li, Y. Guo, *Electrochim. Acta*, 54 (2009) 3303.
12. M. Zhu, G. Sun, Q. Xin, *Electrochim. Acta*, 54 (2009) 1511.
13. Sh. Yin, Z. Wang, X. Qian, D. Yang, Y. Xu, X. Li, L. Wang, H. Wang, *ACS Sustainable Chem. Eng.*, 7 (2019) 7960.
14. V.S. Murthi, R.C. Urian, S. Mukerjee, *J. Phys. Chem. B*, 108 (2004) 11011.
15. V. Jalan, E.J. Taylor, *J. Electrochem. Soc.*, 130 (1983) 2299.
16. B.C. Beard, P.N. Ross, *J. Electrochem. Soc.*, 137(1990) 3368.
17. S. Mujkerjee, S. Srinivasan, M.P. Soriaga, J. McBreen, *J. Electrochem. Soc.*, 142 (1995) 1409.
18. T. Toda, H. Igarashi, H. Uchida, M. Watanabe, *J. Electrochem. Soc.*, 146 (1999) 3750.
19. X. Deng, F. Galli, M.T.M. Koper, *ACS Appl. Energy Mater.*, 3 (2020) 597.
20. E. Antolini, J.R.C. Salgado, M.J. Giz, E.R. Gonzalez, *Int. J. Hydrogen Energy*, 30 (2005) 1213.
21. V. Stamenkovic, B.S. Moon, K.J.J. Maryhofer, P.N. Ross, N.N. Markovic, J. Rossmeisl, J. Greeley, J.K. Norskov, *Angew. Chem. Int. Ed.*, 45 (2006) 2897.
22. J.K. Norskov, J. Rossmeisl, A. Longadottir, L. Lindqvist, *J. Phys. Chem. B*, 108 (2004) 17886.
23. Table 3.14.13. *Department of Energy*. http://www.eere.energy.gov. (2011)
24. *Japanese New Energy and Industrial Technology Development Organization (NEDO)* http://www.nedo.go.jp/english/index.html. (2013)
25. *Fuel Cells and Hydrogen Joint Undertaking, European Commision* http://www.fch-ju.eu (2013)
26. R. Ghosh, S. Paria, *Chem. Rev.*, 112 (2012) 2373.
27. M. Oezaslan, F. Hasche, P. Strasser, *J. Phys. Chem. Lett.*, 4 (2013) 3273.
28. Y. Wang, J.W. Ren, K. Deng, L.L. Gui, Y.Q. Tang, *Chem. Mater*, 12 (2000) 1622
29. E. Zagoraiou, N. Shroti, M.K. Daletou, *Mater. Today Chem.*, 16 (2020) 100263.
30. X. Yan, H. Liu, K.Y. Liew, *J. Mater. Chem.*, 11 (2001) 3387.
31. M. Farsadrooh, M. Z. Yazdan-Abad, M. Noroozifar, H. Javadian, N. Alfi, A.R. Modarresi-Alam, *Int. J. Hydrogen Energy*, 45 (2020) 27312.
32. W. Zhou, Z. Zhou, Sh. Song, W. Li, G. Sun, P. Tsiakaras, Q. Xin, *Appl. Catal., B*, 46 (2003) 273.
33. M. González-Hernández, E. Antolini, J. Perez, *Catalysts*, 9 (2019) 61.
34. W. Li, Ch. Liang, W. Zhou, J.S. Qiu, Z.H. Zhou, G.Q. Sun, Q. Xin, *J. Phys. Chem.*, 107 (2003) 6292.
35. W. Li, W. Zhou, H. Li, Zh. Zhou, B. Zhou, G. Sun, Q. Xin, *Electrochim. Acta*, 49 (2004) 1045.
36. B. Ulas, A. Kivrak, N. Aktas, H. Kivra, *Fullerenes Nanotubes Carbon Nanostruct.*, 27 (2019) 545.
37. M. Tsuji, M. Hasimoto, N. Nishizawa, M. Kubokawa, T. Tsuji, *Chem. Eur. J.*, 11 (2005) 440.
38. I. Bilecka, M. Niederberger, *Nanoscale*, 2 (2010) 1358.

39. Z. Lalegani, S.A. Seyyed Ebrahimi, B. Hamawandi, L. La Spada, M.S. Toprak, Optical Materials, 108 (2020) 110381.
40. M. Karimipour, E. Shabani, M. Mollaei, *J. Nanopart. Res.*, 17 (2015) 1.
41. Z. Zhao, X. Zhang, H. Zhou, G. Liu, M. Kong, G. Wang, *Microporous Mesoporous Mater.*, 242 (2017) 50.
42. D.V. Pryazhnikov, O.O. Efanova, M.S. Kiseleva, I.V. Kubrakova, *Nanotechnol. Russ.*, 12 (2017) 199.
43. J. Penga, Z. Penga, Z. Zhua, R. Augustineb, M.M. Mahmoud, H. Tanga, M. Raoa, Y. Zhanga, G. Lia, T. Jiang, *Ceram. Int.*, 44 (2018) 21015.
44. P. Strasser, S. Kühl, *Nano Energy*, 29 (2016) 166
45. F. Gloaguen, F. Andolfatto, R. Durand, P. Ozil, *J. Appl. Electrochem.*, 24 (1994) 8639.
46. I. Takahashi, S.S. Kocha *J. Power Sources*, 195 (2010) 6312.
47. Y. Garsany, I.L. Singer, K.E. Swider-Lyons, *J. Electroanal. C*hem., 662 (2011) 396.
48. Y. Garsany, O.A. Baturina, K.E. Swider-Lyons, S.S. Kocha, *Anal. Chem.*, 82 (2010) 6321.
49. Y. Garsany, J. Ge, J. St- Pierre, R. Rocheleau, K.E. Swider-Lyons, *ECS Trans.*, 58 (2013) 3.
50. B.G. Pollet, *Electrocatalysis*, 5 (2014) 330.
51. B.G. Pollet, J.T.E. Goh, *Electrochim. Acta*, 128 (2014) 292.
52. B.G. Pollet *Int. J. Hydrogen Energy*, 35 (2010) 11986.
53. Sh Ali, R. Ahmed, M. Sohail, S.A. Khan, M. Sh. Ansari, *J. Ind. Eng. Chem.*, 28 (2015) 344.
54. A.R. West, *Solid State Chemistry and its applications*, Wiley, New York (1984)
55. V. Radmilovik, H.A. Gasteiger, P.N. Ross Jr, *J. Catal*, 154 (1995) 98.
56. S. Beyhan, N.E. Sahin, S. Pronier, J.M. Leger, F. Kadirgan, *Electrochim. Acta*, 151 (2015) 565.
57. R. Lin, Ch. Cao, T. Zhao, Z. Huang, B. Li, A. Wieckowski, J. Ma, *J. Power Sources*, 223 (2013) 190.
58. K.A. Kuttiyiel, K. Sasaki, Y. Choi, D. Su, P. Liu, R.R. Adzic, *Nano Lett.*, 12 (2012) 6266.
59. T.J. Schmidt, H.A. Gasteiger, D.G. Stäb, P.M. Urban, D.M. Kolb, R.J. Behm, *J. Electrochem. Soc.*, 145 (1998) 2354.
60. P. Convert, C. Coutanceau, P. Crouigneau, F. Gloaguen, C. Lamy, *J. Appl. Electrochem.*, 31 (2001) 945.
61. N.M. Markovic, H.A. Gasteiger, B.N. Grgur, P.N. Ross, *J. Electronal. Chem.*, 467 (1999) 157.
62. C. Coutanceau, M.J. Croissant, T. Napporn, C. Lamy, Electrochim. Acta, 46 (2000) 579.
63. A. Holewinski, S.J. Linic, *J. Electrochem. Soc.*, 159 (2012) H864.
64. J. Wang, F.A. Uribe, T.E. Springer, J Zhang, R.R. Adzic, *Faraday Disc*, 140 (2009) 347.
65. M. Oezaslan, P. Strasser, *J. Power Sources*, 196 (2011) 5240.
66. S. Ozenler, N. Sahin, B. Akaydin, L. Ovecoglu, A. Genc, J.M. Leger, T.W. Napporn, F. Kadirgan, *ECS Trans.*, 41 (2011) 1031.
67. H. Wang, X. Yuan, D. Li, X. Gu, *J. Colloid Interface Sci.*, 384 (2012) 105.
68. D. Wang, H.L. Xin, R. Hovde, H. Wang, Y. Yu, D.A. Muller, F.J. Disalvo, H.D. Abruña, *Nat. Mater.*, 12 (2013) 81.
69. X. Zhong, L. Wang, H. Zhou, Y. Qin, W. Xu, Y. Jiang, Y. Sun, Z. Shi, G. Zhuang, X. Li, D. Mei, J.G. Wang, *Adv. Mater. Interfaces*, 2 (2015) 1500365.
70. Sh. Hu, M. Tian, E.L. Ribeiro, G. Duscher, D. Mukherjee, *J. Power Sources*, 306 (2016) 413.
71. Y. Qin, X. Zhang, X. Dai, H. Sun, Y. Yang, X. Li, Q. Shi, D. Gao, H. Wang, N.F. Yu, Sh.G. Sun, *Small*, 12 (2016) 524.
72. N.E. Sahin, T.W. Napporn, L. Dubau, F. Kadirgan, J.M. Léger, K.B. Kokoh, *Appl. Catal., B,* 203 (2017) 72.
73. H. Yano, M. Watanabe, A. Liyama, H. Uchida, *Nano Energy*, 29 (2016) 323.
74. Q. Wan, S. Hu, J. Dai, Ch. Chen, W.X. Li, *J. Phys. Chem. C*, 123 (2019) 11020.
75. P. Kanninen, B. Eriksson, F. Davodi, M.E. Melandso Buan, O. Sorsa, T. Kallio, R. Wreland, *Electrochim. Acta*, 332 (2020) 135384.

76. M.H. Lee, P.S. Wang, J.S. Do, *J. Solid State Electrochem.*, 12 (2008) 879.
77. P.T. Yu, W. Gu, R. Makharia, F.T. Wagner, H.A. Gasteiger, *ECS Trans.*, 3 (2006) 797.
78. R.A. Moghadam Esfahani, R.B. Moghaddam, I.I. Ebralidze, E. Bradley Easton, *Appl. Catal., B*, 239 (2018) 125.
79. T. Ioroi, Z. Siroma, N. Fujiwara, S. Yamazaki, K. Yasuda, *Electrochem. Commun.*, 7 (2005) 183.